

## Optimal trace selection for AVA processing of shale-sand reservoirs

Thomas Guest<sup>1</sup> and Andrew Curtis<sup>1</sup>

### ABSTRACT

When processing data, a principal aim is to maximize information inferred from a data set by minimizing the expected postprocessing uncertainties on parameters of interest. Nonlinear statistical experimental design (SED) methods can be used to find optimal trace profiles for processing amplitude-variation-with-angle (AVA) surveys that account for all prior petrophysical information about the target reservoir. Optimal selections change as prior knowledge of rock parameters and reservoir fluid content changes, and which of the prior parameters have the greatest effect on selected traces can be assessed. The results show that optimal profiles are far more sensitive to prior information about reservoir porosity than to information about saturating fluid properties. By applying ray-tracing methods, AVA results can be used to design optimal processing profiles from seismic data sets for multiple targets, each with different prior-model uncertainties.

### INTRODUCTION

Huge sums of money are invested every year in geophysical surveys and experiments. Prior to data collection, every survey or experiment must be planned. After the raw data have been collected, a data-processing workflow is designed and performed to infer properties of the earth's subsurface. These planning stages take into consideration any physical and logistical constraints that place boundaries on the types of experiments that are feasible and on the range of applicable processing techniques. Within these constraints, maximizing the amount of information recorded during the experiment and inferred postprocessing often trades off with minimizing cost. For this reason, optimizing designs of experiments in terms of cost, logistics, and the information which the experiments are expected to provide becomes of critical importance to maximizing return on investment (Maurer and Boerner, 1998; Curtis and Maurer, 2000).

Statistical experimental design (SED) is a field of statistics devoted

to developing methods of designing experiments to maximize information, typically by minimizing the predicted postexperimental uncertainties on parameters of interest while satisfying other practical constraints. However, in many of the geosciences, the design process is typically carried out by using relatively inaccurate heuristics (rules of thumb) rather than SED methods. In geophysics, in which enormous sums are spent on data collection, formal SED theory has been used only to optimize designs in certain cases: designing of tomographic surveys (Barth and Wunsch, 1990; Curtis, 1999a, b; Curtis et al., 2004), earthquake monitoring surveys (Kijko, 1977a, b; Steinberg et al., 1995; Rabinowitz and Steinberg, 2000; Winterfors and Curtis, 2008), microseismic monitoring surveys (Curtis et al., 2004), resistivity surveys (Maurer et al., 2000; Stummer et al., 2004; Furman et al., 2004; Furman et al., 2007; Wilkinson et al., 2006; Coles and Morgan, 2009), geologic expert elicitation processes (Curtis and Wood, 2004), time-lapse surveys (Oldenborger et al., 2007; Ajo-Franklin, 2009; Oldenborger and Routh, 2009), and amplitude-versus-offset experiments (van den Berg et al., 2003; Guest and Curtis, 2009). (See Curtis 2004a, b for a review of SED related to the geosciences.)

No one has yet applied SED to design industrial-scale surface-seismic surveys or their postacquisition processing. This paper takes a significant step in that direction by showing how to select optimal data subsets to process after an experiment or survey has been performed, to maximize the information inferred from the recorded data while minimizing processing cost.

We treat the problem of data subset selection or design in the SED framework because those methods are equally applicable in this context. Optimal experimental design methods can be used (1) to plan the data-collection phase so that unnecessary data that provide little information are not recorded, or (2) in the data-processing phase, in which only the recorded data that provide significant information about the parameters of interest are selected and processed. The term *optimal design*, used subsequently, can refer to designing the survey or designing the data subset for processing.

To design experiments optimally requires an understanding of the physical relationships linking the recorded data and postexperimental parameter uncertainties (Box and Lucas, 1959; Atkinson and

Manuscript received by the Editor 12 May 2009; revised manuscript received 23 February 2010; published online 22 September 2010.

<sup>1</sup>University of Edinburgh, School of GeoSciences, Grant Institute, and Edinburgh Collaborative of Subsurface Science and Engineering (ECOSSE), U. K. E-mail: t.e.guest@sms.ed.ac.uk; andrew.curtis@ed.ac.uk.

© 2010 Society of Exploration Geophysicists. All rights reserved.

Donev, 1992). Let function  $\mathbf{F}_\xi$  represent the relationship between parameters  $\mathbf{m}$  and data  $\mathbf{d}$ , such that if we ignore measurement error for now,

$$\mathbf{d} = \mathbf{F}_\xi(\mathbf{m}) \quad (1)$$

would be recorded if parameters  $\mathbf{m}$  correctly represented reality. Subscript  $\xi$  in the forward function  $\mathbf{F}_\xi$  indicates that the parameter-data relationship is dependent either on the experimental design  $\xi$ , in which  $\xi$  is a vector representing, for example, source and receiver types and locations, or on the data subset processed, in which  $\xi$  would represent that subset. In this study, we invoke the latter definition of  $\xi$ .

One of the principal reasons that SED theory has not gained general acceptance in the geosciences is that the forward function  $\mathbf{F}_\xi$  is commonly highly nonlinear. The results of applying linearized SED theory therefore are not robust, whereas applying fully nonlinear methods is considered to be too computationally costly. As a result, in all the references above, only the work of van den Berg et al. (2003), Winterfors and Curtis (2008), and Guest and Curtis (2009) apply fully nonlinear design theory. Of these works, van den Berg et al. (2003) addressed only a single-parameter vector and Winterfors and Curtis (2008) a 2D parameter vector. Guest and Curtis (2009) introduced a novel methodology based on a Bayesian framework of sequentially increasing the parameter vector until a high-dimensional experiment has been designed without any linearization of the physical models. This work has made it computationally feasible to apply a nonlinear SED method to geophysical survey design with multiple data and is also applicable to data-selection problems. Therefore, it should increase the uptake of such methods in the geosciences.

In this paper, we focus on applying the method of Guest and Curtis (2009) to designing optimal trace-selection profiles for processing amplitude-variation-with-angle (AVA) surveys for sand-clay reservoir models in which some, perhaps limited, prior petrophysical information about the subsurface is known. We examine how the optimal trace-selection designs change as our prior knowledge of rock parameters and reservoir fluid content changes, and we assess which of the prior parameters have the greatest effect on trace-selection designs and therefore are deemed the most important to bound as tightly as possible prior to the survey. The resulting trace selections can be used to select a subset of traces to process or, if all traces are to be processed, to decide which traces deserve most of the processor's attention to reduce noise and which should be given less attention. An overview of the Guest and Curtis (2009) method is given below, but we refer the reader to the original work for a detailed explanation.

## EXPERIMENTAL DESIGN METHOD

The method of Guest and Curtis (2009) can be divided into three parts. First, a Bayesian quality metric is defined that quantifies the information provided by any given trace-subset (design). Second, an iterative method sequentially increases the complexity of the trace subset so as to maximally increase the quality. Third, a numerical sampling scheme minimizes the computational time required to calculate the best design at each iteration. Each of these three parts is presented briefly below from the point of view of selecting optimal data subsets for processing.

## Bayesian design method

Let  $\rho(\mathbf{m})$  be the probability density function (pdf) representing the prior information on parameters of interest  $\mathbf{m}$ . If new data are recorded in a survey and data subset  $\mathbf{d}$  designed or defined by parameters  $\xi$  is processed, then according to Bayes' theorem, the postprocessing or so-called posterior pdf of the parameters  $\mathbf{m}$  given data  $\mathbf{d}$  and trace-selection design  $\xi$  is given by

$$\sigma(\mathbf{m}|\mathbf{d},\xi) = \frac{\theta(\mathbf{d}|\mathbf{m},\xi)\rho(\mathbf{m})}{\sigma(\mathbf{d}|\xi)}. \quad (2)$$

Here,  $\theta(\mathbf{d}|\mathbf{m},\xi)$  represents the pdf of data  $\mathbf{d}$  being observed given parameters  $\mathbf{m}$  and selected traces  $\xi$  and includes information in the forward function in equation 1, and  $\sigma(\mathbf{d}|\xi)$  is the marginal distribution over observed data and contains all information about which data are likely to be recorded during the experiment (Tarantola, 2005).

In selecting which data subset  $\xi$  to process, we wish to maximize the information content on the parameters that is expected to be contained within the posterior pdf  $\sigma(\mathbf{m}|\mathbf{d},\xi)$ . Therefore, we need to quantify the information  $I$  represented by this pdf for any particular trace-selection design  $\xi$ . The entropy of any probability distribution  $f(\mathbf{x})$  is related to Shannon's measure of information (Shannon, 1948) according to

$$I\{f(\mathbf{x})\} + c = -\text{Ent}(\mathbf{X}) = -\int_{\mathbf{x}} f(\mathbf{x})\log\{f(\mathbf{x})\}d\mathbf{x}, \quad (3)$$

where Ent is the entropy function (defined on the right),  $f(\mathbf{x})$  is the pdf of the random variable  $\mathbf{X}$ ,  $I$  is the information measure as defined by Shannon (1948), and  $c$  is a constant. For example, if  $f(\mathbf{x})$  is Gaussian with standard deviation  $\tau$ , information  $I = -\frac{1}{2}\log(2\pi e\tau)$ , hence maximizing information  $I$  is equivalent to minimizing uncertainty  $\tau$ . The definition in equation 3 extends this concept of information to pdfs of any form, in which case entropy is a measure of uncertainty analogous to  $\tau$ .

The optimal trace selection corresponds to the trace-selection design that maximizes the information expected to be contained in the posterior parameter pdf (equation 2). Expected postprocessing information on parameters  $\mathbf{m}$  is defined (after Lindley, 1956) using equation 2 and equation 3 to be

$$\varphi(\xi) = -\int_D \text{Ent}\{\sigma(\mathbf{m}|\mathbf{d},\xi)\}\sigma(\mathbf{d}|\xi)d\mathbf{d}, \quad (4)$$

where  $-\text{Ent}\{\sigma(\mathbf{m}|\mathbf{d},\xi)\}$  represents the amount of information contained in the posterior pdf about the parameters  $\mathbf{m}$  given a particular data measurement  $\mathbf{d}$  and trace-selection design  $\xi$ . The quality measure is calculated by taking the expectation of the entropy function with respect to the marginal distribution ( $\sigma(\mathbf{d}|\xi)$ ) over all data measurements.

However, in many cases evaluating  $\sigma(\mathbf{m}|\mathbf{d},\xi)$  in equation 2 and equation 4 represents finding the solution to an inverse problem because it requires that information in data  $\mathbf{d}$  on the left of equation 1 be translated into corresponding constraints on parameters  $\mathbf{m}$ . In nonlinear problems, this can be computationally demanding. However, Shewry and Wynn (1987) show that design measure  $\Phi(\xi)$  obeys the identity

$$-\Phi(\xi) + \text{Ent}\{\sigma(\mathbf{d}|\xi)\} = \text{Ent}\{\sigma(\mathbf{d},\mathbf{m}|\xi)\} = b, \quad (5)$$

where  $b$  is a constant, and the second equality is true if both the prior parameter pdf  $\rho(\mathbf{m})$  and the noise or uncertainty on the data measurements are expected to be design independent.

In reality, the measurement noise might not be completely design

independent, but the assumption often is made nevertheless because in many practical cases, it is assumed that the parameter-data relationship is of the form

$$\mathbf{d} = \mathbf{f}_{\xi}(\mathbf{m}) + \boldsymbol{\varepsilon}, \quad (6)$$

where  $\boldsymbol{\varepsilon}$  is a vector of independent random errors which do not depend on the parameters or on the trace-selection design. Under this assumption, equation 5 shows that an optimal trace-selection design can be found by maximizing  $\text{Ent}\{\sigma(\mathbf{d}|\xi)\}$ , because this ensures that  $\Phi(\xi)$  is maximized. Evaluating this former measure only requires information about the pdf  $\sigma(\mathbf{d}|\xi)$ . This pdf represents information about the data set expected to be recorded, which can be calculated in most cases by projecting the prior information on the parameters through the physical forward relationship  $\theta(\mathbf{d}|\mathbf{m},\xi)$ . Hence, this requires only that the forward function (rather than the inverse problem) be solved.

Altering trace selection  $\xi$  changes the properties of the forward function (equation 6) and the properties of the pdf  $\sigma(\mathbf{d}|\xi)$  and therefore its entropy value. The selected trace combination that corresponds to the maximum entropy value also corresponds to maximum expected information about  $\mathbf{m}$  and hence to the optimal experimental design.

## Sequential design

When there are multiple design parameters — in our case, traces or angles of incidence — searching the entire design space (the space of all permissible combinations of design parameters) is computationally infeasible. Guest and Curtis (2009) introduced a novel iteratively constructive design strategy which sequentially increases the number of elements within the design vector  $\xi$  by one element at each iteration,

$$\xi_j = \arg \max[\text{Ent}\{\sigma(\mathbf{d}|\xi_j)\}], \text{ such that } \xi_{j-1} \text{ is fixed} \quad (7)$$

where  $\xi_j = \{\xi^1, \dots, \xi^j\}$  and  $\xi^i$  is an element of the trace-selection design vector. The new optimal trace-selection design  $\xi_j$  combines the data defined at the previous iteration  $\xi_{j-1}$ , augmented by the single datum defined by  $\xi^j$  that maximizes the entropy of the posterior data pdf, given that  $\xi_{j-1}$  remains fixed. In this way, the total work required to design an experiment with 10 selected traces is reduced from searching a 10D design space to 10 separate searches of a 1D design space. Although the trace-selection design at each iteration is then only a locally optimal design, Guest and Curtis (2009) show that for problems in amplitude variation with offset (AVO) or AVA, the locally optimal design is almost identical to the globally optimal design in cases in which the latter was computationally viable to calculate.

## Numerical sampling scheme

In general, the pdf required to calculate the entropy is not known analytically and therefore must be calculated numerically. Samples of  $\rho(\mathbf{m})$ , the prior pdf describing what is known about the subsurface before the experiment, are generated and projected through the physical relationship (equation 6), which also incorporates measurement error ( $\boldsymbol{\varepsilon}$ ), to produce samples of  $\sigma(\mathbf{d}|\xi)$  in the (discretized) data space. The resulting histogram is normalized to have unit volume, after which it represents a numerical approximation to the pdf  $\sigma(\mathbf{d}|\xi)$ . This numerical approximation of  $\sigma(\mathbf{d}|\xi)$  then can be used to assess the quality of the experimental design by calculating the entropy,

$$\text{Ent}\{\sigma(\mathbf{d}|\xi)\} \approx \sum_i \hat{\sigma}(\mathbf{d}_i) \log\{\hat{\sigma}(\mathbf{d}_i)\}, \quad (8)$$

where  $\mathbf{d}_i$  represents the center of the  $i$ th discretized bin in the data space. For any given experimental design, the estimate of  $\hat{\sigma}(\mathbf{d}|\xi)$  is affected by the number of parameter samples, the data-space discretization bin size, and the measurement error.

With each iteration of equation 7, the data space increases by one dimension. For example, in a seismic AVA survey, the reflection coefficient recorded for a given interface at each receiver represents a single dimension. As successive receivers are selected to be processed, the number of data-space dimensions increases and therefore so does the number of model samples required to accurately approximate the posterior pdf  $\sigma(\mathbf{d}|\xi)$ . As more samples are added to approximate equation 8, the calculated entropy value becomes more accurate and will asymptote to a final value. Guest and Curtis (2009) introduce a scheme that measures this change in entropy value for several trace-selection designs which span the entire design space. For each of the selected designs, the standard deviation of the entropy value is calculated over a specific range of additional samples, with the maximum entropy value becoming the so-called test value. The optimal trace-selection design result is reached when only one entropy maximum in the design space is found within the error range of the test value. Using the same approach, trace-selection designs that have an entropy value lower than a predefined threshold, also derived from the test value, are removed from the current iteration to reduce the size of the design space that must be searched.

Figure 1 shows a flowchart of how the design methods are combined to select an additional design parameter. First the prior-model pdf, the range of possible designs to be considered, and the variable  $ns$  representing the maximum number of model evaluations that are computationally tractable at each iteration are selected. For each possible design,  $ns$  random samples of the prior model pdf are projected into the discretized data space. The density of the resulting data

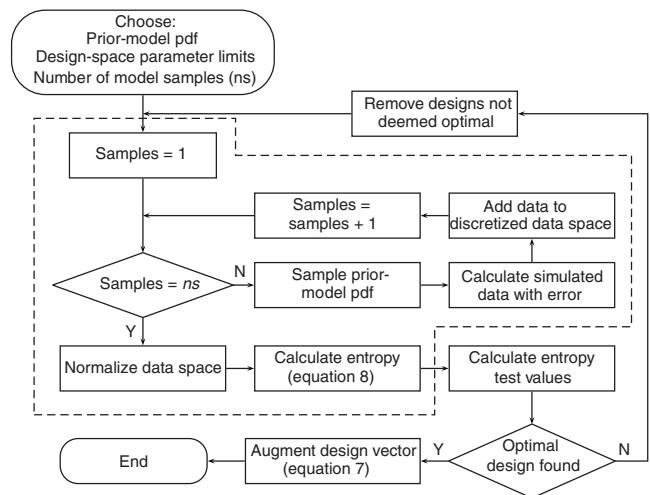


Figure 1. Flowchart showing how an additional design parameter is chosen. The workflow inside the dotted line is performed simultaneously for all possible designs. With each iteration that the entropy test value is calculated, the design space is reduced by removing designs that are deemed never to be optimal. The required value of  $ns$ , the number of times the prior-model pdf should be sampled before the data space is normalized, is dependent on the forward function and the prior-model pdf. The initial design-space prior-model parameter ranges should be identical for each run through the sequential design process.

ta-space samples for each design are normalized so that they represent numerical approximations of  $\sigma(\mathbf{d}|\xi)$ . The entropy is then calculated for each possible design using equation 8. A statistical test is performed to calculate whether the result is likely to be optimal in the sense that it represents a statistically significant maximum above the level of numerical random-sampling noise. If so, the design corresponding to that maximum is deemed optimal, and the process is stopped. If it is not deemed optimal, then designs that fall below a predefined entropy threshold are removed and an additional set of  $ns$  random samples is projected from the prior-model pdfs into the discretized data spaces. The process is repeated until a statistically significant optimal design has been found.

### RESERVOIR APPLICATION: SELECTING OPTIMAL TRACES FOR AMPLITUDE-VARIATION-WITH-ANGLE (AVA) PROCESSING

#### AVA design method

The amplitude of an incoming seismic wave with unit amplitude which is reflected from a subsurface boundary between two geologic layers at depth  $d$  (Figure 2) is a function of the incident angle of the wave at the boundary, density  $\rho$ , and the elastic media properties

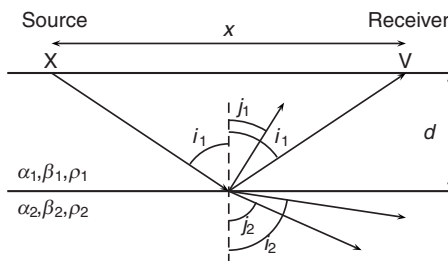


Figure 2. Geometry of an AVA experiment with a single interface at depth  $d$ . The distance between the source (X) and the receiver (V) is called the offset ( $x$ ). At the interface, P-wave energy incident at angle  $i_1$  is split into a reflected P-wave (angle  $i_1$ ) and a P-S wave conversion (angle  $j_1$ ) and is transmitted into the second layer as a P-wave (angle  $i_2$ ) and P-S wave conversion (angle  $j_2$ ). Amplitudes of each wave are given by equations 9. Properties of the subsurface are density ( $\rho$ ), P-wave velocity ( $\alpha$ ), and S-wave velocity ( $\beta$ ) in each of layers 1 and 2.

Table 1. Rock parameters required for the Goldberg and Gurevich (1998) model.<sup>a</sup>

Parameter	Range
Sand bulk modulus (GPa)	36–43
Sand shear modulus (GPa)	33–46
Sand density ( $\text{kg}/\text{m}^3$ )	2640–2650
Clay bulk modulus (GPa)	20–34
Clay shear modulus (GPa)	7–19
Clay density ( $\text{kg}/\text{m}^3$ )	2350–2680
Reservoir porosity (%)	10–40
Clay content (%)	20–50

<sup>a</sup>Ranges represent the extreme values of the uniform prior pdfs that were used to create velocity and density models. Extreme values are taken from Marion et al. (1992), Mavko et al. (1998), Carcione et al. (2003), and Chen and Dickens (2009). The values shown represent grain properties rather than dry matrix properties.

(summarized by the P-wave velocity  $\alpha_i$  and S-wave velocity  $\beta_i$  for an isotropic medium) of both layers  $i = 1, 2$ . The recorded amplitudes of the reflected waves (after the effects of geometric spreading have been accounted for) are given by the solution to the Zoeppritz equations (Zoeppritz, 1919):

$$\begin{aligned} & \cos i_1 A_1 + \frac{\alpha_1}{\beta_1} \sin j_1 B_1 + \frac{\alpha_1}{\alpha_2} \cos i_2 A_2 - \frac{\alpha_1}{\beta_2} \sin j_2 B_2 \\ & = \cos i_1 \\ & -\sin i_1 A_1 + \frac{\alpha_1}{\beta_1} \cos j_1 B_1 + \frac{\alpha_1}{\alpha_2} \sin i_2 A_2 + \frac{\alpha_1}{\beta_2} \cos j_2 B_2 \\ & = \sin i_1 \\ & -\cos 2j_1 A_1 - \sin 2j_1 B_1 + \frac{\rho_2}{\rho_1} \cos 2j_2 A_2 - \frac{\rho_2}{\rho_1} \sin 2j_2 B_2 \\ & = \cos 2j_1 \\ & \sin 2i_1 A_1 - \frac{\alpha_1^2}{\beta_1^2} \cos 2j_1 B_1 + \frac{\rho_2 \beta_2^2 \alpha_1^2}{\rho_1 \beta_1^2 \alpha_2^2} \sin 2i_2 A_2 + \frac{\rho_2 \alpha_1^2}{\rho_1 \beta_1^2} \\ & \quad \times \cos 2j_2 B_2 = \sin 2i_1 \end{aligned} \quad (9)$$

where for a horizontal boundary,  $i_1$  is the P-wave angle of incidence and reflection,  $i_2$  the P-wave angle of refraction,  $j_1$  the converted P-S-wave angle of reflection, and  $j_2$  the converted P-S-wave angle of refraction. The amplitudes of the waves are represented by  $A_1$  for the reflected P-wave,  $A_2$  for the refracted P-wave,  $B_1$  for the reflected S-wave, and  $B_2$  for the refracted S-wave. From measurements of the reflected P-wave amplitude at a range of offsets  $i_1$ , it is possible to obtain information about the elastic media properties ( $\alpha_2$  and  $\beta_2$ ) and density ( $\rho_2$ ) of the lower layer

$$A_1(i_1) = f_x(\alpha_2, \beta_2, \rho_2; i_1). \quad (10)$$

The design problem that we address here is to find the optimal subset of incident angles ( $i_1$ ) that best constrains these values of the parameters given the recorded P-wave reflection coefficients. By ray-tracing to the surface, these angles define the optimal subset of traces to be analyzed because they are expected to contain maximum information about the subsurface parameters of the lower layer (e.g., a reservoir).

#### Reservoir model

To calculate the posterior pdf  $\sigma(\mathbf{d}|\xi)$  where  $\mathbf{d}$  represents the P-wave reflection coefficient requires prior distributions over  $\alpha$ ,  $\beta$ , and  $\rho$  for both geologic layers. We assume that the overburden is a shale with known  $\alpha = 3048$  m/s,  $\beta = 1244$  m/s, and  $\rho = 2400$   $\text{kg}/\text{m}^3$ , the same overburden model used by Ostrander (1984) to analyze plane-wave reflection coefficients as a function of incidence angle for a reservoir model. The corresponding values for the reservoir (the lower geologic layer) are unknown. In other situations, the values for the overburden might also be varied without otherwise changing the methods used here. In this study, however, we wish to highlight how the optimal trace-selection designs depend on expected reservoir properties, so we hold the overburden fixed.

We build a reservoir model by assuming that the semiempirical petrophysical model of Goldberg and Gurevich (1998) is valid for sand-shale reservoirs with different saturating fluids. For any particular reservoir rock-physics properties (e.g., sand and shale proportions, porosities, fluid content, etc.; see Tables 1 and 2), the Goldberg and Gurevich (1998) model calculates corresponding P-wave and S-

wave velocities and density values. These can be used in conjunction with the Zoeppritz equations (equation 9) to calculate a P-wave reflection coefficient. By assuming prior uncertainty ranges over the properties in Tables 1 and 2, prior parameter pdfs of the P-wave and S-wave velocity and density can be constructed and used to determine the optimal trace-selection design, given the various prior uncertainty ranges. The prior uncertainty ranges for the matrix bulk properties are shown in Table 1. Three fluid properties are considered (Table 2) independently to observe how the optimal trace-selection design changes for different saturating fluids. We assume uniform pdfs over all parameter ranges; however, the method allows the prior information ( $\rho(\mathbf{m})$ ) to be represented by any type of distribution such as Gaussian or Cauchy.

Figure 3 shows crossplot histograms of the models produced from 1,000,000 random samples from these uniform distributions, using the properties of brine (Figure 3a-c), oil (Figure 3d-f), and gas (Figure 3g-i) as the saturating fluid. Figure 3 illustrates that from the uniform ranges in Tables 1 and 2, a large variety of velocity and density models can be created.

Figure 4a shows the P-wave reflection-coefficient histogram for the brine-saturated reservoir model generated from 1,000,000 samples at incident angles ranging from 0° to 90° calculated using the Zoeppritz equations. For AVA modeling, the Zoeppritz equations are relatively cheap to compute. If a more complex forward function is used, it might be computationally infeasible to use as many as 1,000,000 samples. Clearly, the posterior pdf  $\sigma(\mathbf{d}|\xi)$  and therefore the corresponding entropy value will be different for each incident angle at which the amplitude is measured. The incident angle that corresponds to the maximum entropy value represents the optimal angle at which to select data for processing to maximally reduce the expected uncertainties on parameters  $\alpha_2$ ,  $\beta_2$ , and  $\rho_2$ . Then these can be used to constrain the bulk rock and fluid properties of the reservoir.

Assuming different saturating fluid parameters (Table 2) results in different velocity and density profiles and therefore different reflection-coefficient signatures. As one would predict, changing the saturating fluid from brine to oil to gas (Figure 3) results in a progressively lower reservoir density. For all three fluids, however, the overall P-wave and S-wave velocity ranges remain very similar. Figure 4 shows the corresponding P-wave reflection-coefficient histograms for the brine, oil, and gas reservoirs.

In the above reservoir models, a uniform porosity ranging from 10% to 40% has been used. To assess the importance of accurately estimating the porosity of the target reservoir when selecting which traces provide the maximum information, we separately consider a low-porosity oil reservoir with a uniform porosity prior pdf distribution ranging from 10% to 20%, a medium-porosity oil reservoir with a uniform prior pdf ranging from 20% to 30%, and a high-porosity oil reservoir with a uniform prior pdf ranging from 30% to 40%.

Figure 5 shows the velocity and density histograms for the oil-saturated reservoir models with varying porosity ranges while keeping the other parameters within the same ranges as those given in Tables

**Table 2. Fluid parameters required for the Goldberg and Gurevich (1998) model.<sup>a</sup>**

Parameter	Range
Brine bulk modulus (GPa)	2.4–3.2
Oil bulk modulus (GPa)	0.5–0.75
Gas bulk modulus (GPa)	0.01
Brine density (kg/m <sup>3</sup> )	1040–1090
Oil density (kg/m <sup>3</sup> )	616–738
Gas density (kg/m <sup>3</sup> )	100

<sup>a</sup>Ranges represent the extreme values of the uniform prior pdfs that were used to create velocity and density models. Values are taken from Clark (1992), Carcione et al. (2003), and Chen and Dickens (2009).

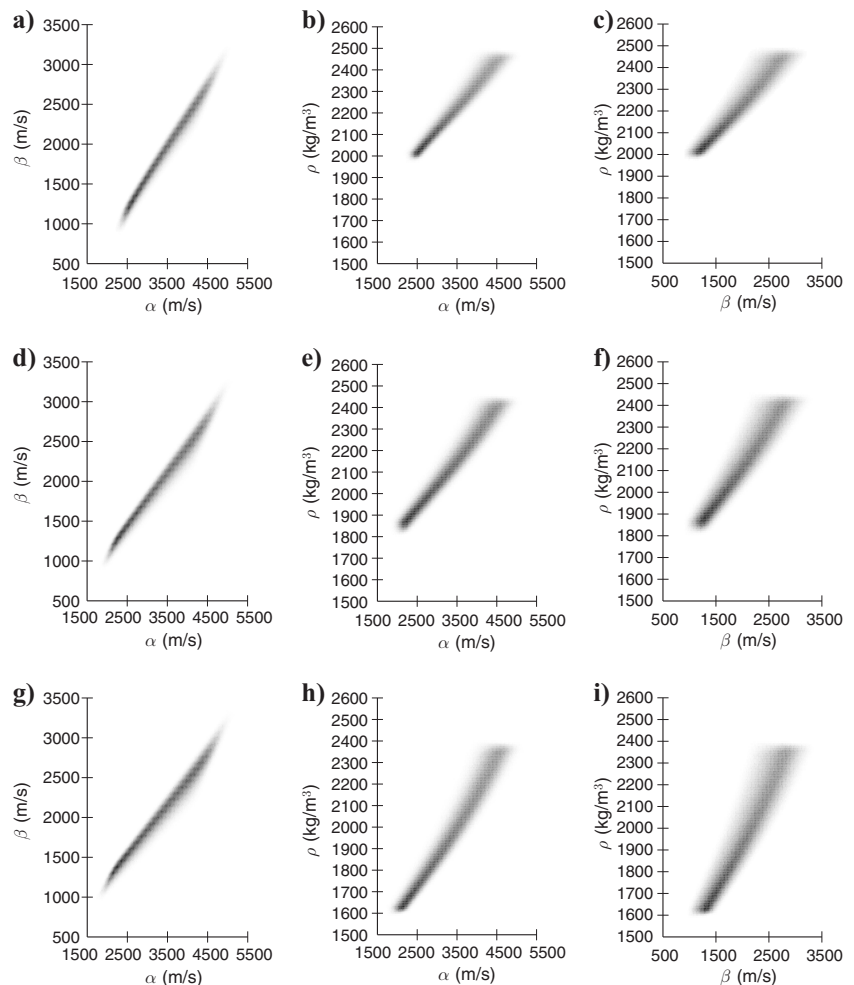


Figure 3. Velocity and density histograms produced for (a-c) a brine-filled reservoir, (d-f) an oil-filled reservoir, and (g-i) a gas-filled reservoir using the uniform parameter ranges in Table 1 and Table 2. Shading represents histogram frequency.

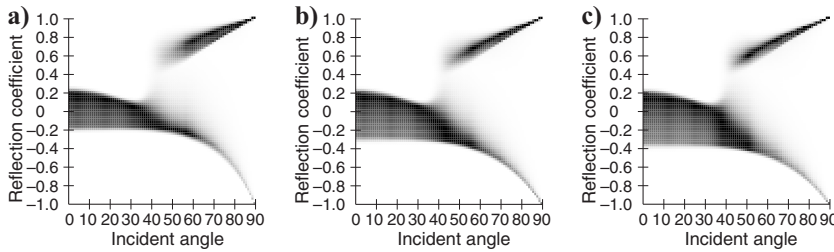


Figure 4. Reflection-coefficient histogram corresponding to the (a) brine-, (b) oil-, and (c) gas-saturated reservoir histograms in Figure 3. The overburden is assumed to be a shale with  $\alpha = 3048$  m/s,  $\beta = 1244$  m/s, and  $\rho = 2400$  kg/m<sup>3</sup>. Darker shading corresponds to more likely reflection coefficients.

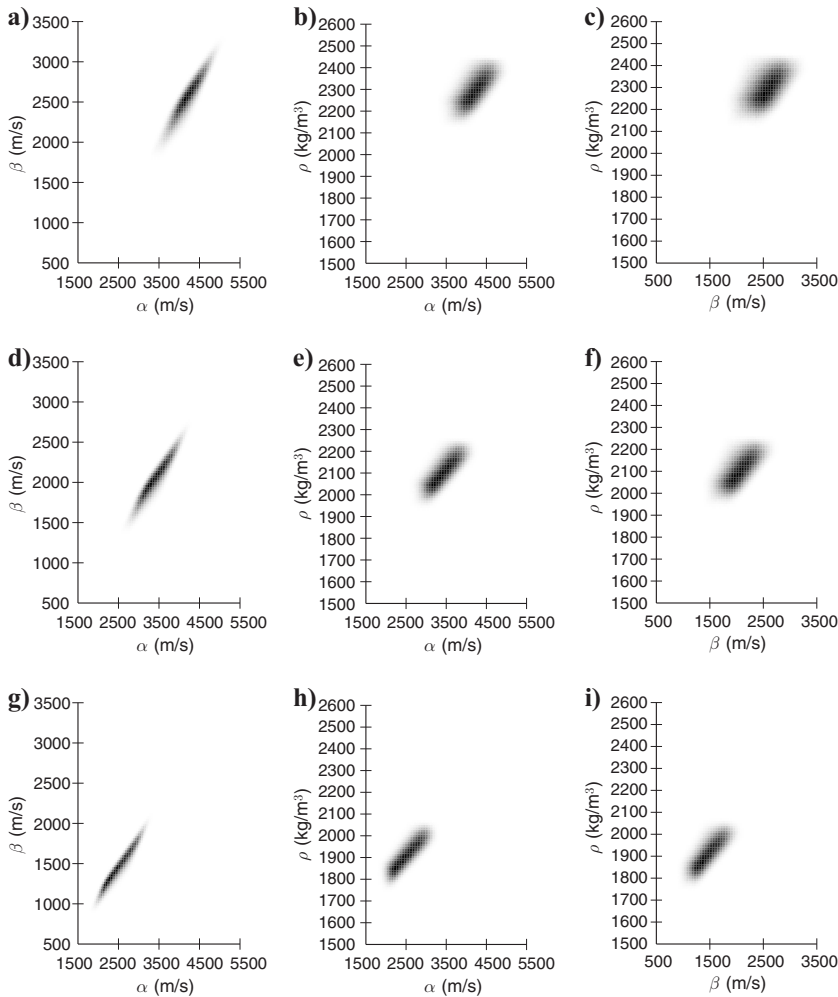
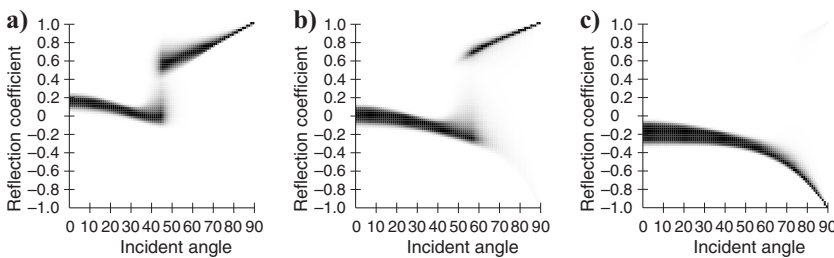


Figure 5. Velocity and density histograms for an oil-filled reservoir with varying uniform prior porosity ranges. Plots (a-c) represent a reservoir with a porosity range of 10% to 20%, (d-f) 20% to 30%, and (g-i) 30% to 40%. Shading represents histogram frequency.



1 and 2. The porosity range has a large impact on the velocity and density profiles. As porosity increases, both the velocity and density of the reservoir decrease. The velocity and density ranges over which the histograms are spread are much smaller than those in Figure 3, clearly demonstrating that the combination of all of the narrow-porosity range results creates the overall distributions seen in Figure 3d-f. As a result, the corresponding reflection-coefficient histograms shown in Figure 6 show reduced ranges of P-wave reflection coefficients, particularly showing that for a high-porosity reservoir, the critical angle is never reached in any survey. When combined, these results represent the overall porosity histogram shown in Figure 4b.

## RESULTS

### Saturating fluid

Figure 7 shows the entropy of  $\sigma(\mathbf{d}|\xi)$  and hence the expected information about model  $\mathbf{m}$  as a function of incident angle when selecting the first angle (trace) to process. This is plotted for each reservoir model (Tables 1 and 2) corresponding to each of three saturating fluids. For incident angles from 0° to 90° at 0.5° separation, the information value was calculated using 500,000 model space samples. As expected, because all the reflection-coefficient curves were similar (Figure 4), the information curves all show the same general features. All three information curves have a maximum value at approximately 50°, equating to the optimal location of the first angle to process. For angles over 70°, the information value decreases quickly, showing that receivers at very large offset angles provide relatively little information relating to the subsurface in this case. Small incident angles (less than 20°) correspond to large information values, whereas for all three fluids, there is a local minimum at approximately 30°.

Figure 8 shows the extension from a single angle to a design that selects 10 angles as calculated using the iteratively constructive method of Guest and Curtis (2009). As expected, all three plots show optimal trace designs with fairly similar features. In each case, the majority of angles selected for processing are placed between inci-

Figure 6. P-wave reflection-coefficient histograms for oil-filled reservoir velocity-density models with the varying uniform prior porosity ranges in Figure 5. Plot (a) represents the low-porosity reservoir (10% to 20%), (b) medium-porosity reservoir (20% to 30%), and (c) high-porosity reservoir (30% to 40%).

dent angles of 0° to 10° and 40° to 70°. This trend fits with the information profiles in Figure 7, where for the single angle, an information minimum was located between 20° and 40°, and at angles greater than 70° the information declines to the global minimum seen at 90°. It is also evident that in the incident-angle ranges in which angles are selected for processing, the angles are not evenly spaced. In the range of 40° to 70°, in all cases the density decreases with incident angle.

In AVA inversion and processing, techniques have been implemented that use recorded data at postcritical angles (e.g., Macdonald et al., 1987; Williams et al., 2001; Liu and Schmitt, 2003; Downton and Ursenbach, 2006; Skopintseva, 2006). In all the models shown, the critical angle occurs at less than 70°. Beyond that angle, the actual source-receiver offset generally becomes prohibitively large, and as seen in our results, little information about the subsurface would be recorded. Because only a single angle in each scenario in Figure 8 is at an angle greater than 70°, it is expected that reducing the allowed incident-angle range will not have a profound impact on the overall design.

Figure 9 shows the 10-angle design when only incident angles between 0° and 70° are considered. The optimal trace designs show the same characteristics as before. The angle selected to be processed outside the range of 0° to 70° has been relocated to fit in with the general trend of decreasing density within the range of 40° to 70°.

**Porosity**

Figure 10 shows the information values used to select the first angle to process for the oil-reservoir models with different porosities. The maximum and hence the optimal angle selected is very different for each of the three porosity models. As porosity increases, the optimal incident angle also increases until a certain porosity threshold is reached. At porosity values close to this threshold value, the information provided at either large angles (> 60°) or near-vertical incidence (0°) are comparable. Beyond this value, near-offset angles provide more information than large angles, in stark contrast to the low-porosity result. From Figure 5, it can be seen that the prethreshold increase in the optimal incident angle is related to an overall decrease in P-wave velocity, S-wave velocity, and density. The threshold corresponds to the point at which the reflection coefficients cease to exhibit the critical-angle threshold as observed in Figure 6a and b but not in 6c. This shows that in cases in which the critical-angle phenomenon can be sampled, maximum information is obtained by doing so.

The solid line in Figure 10 represents the reservoir model with a prior porosity range of 10% to 40%. This information curve encompasses the peaks of the three separate models. By increasing the prior porosity range, the relative information provided by the small incident angles (relative to the large angles) increases when compared to the reservoir models with the porosity ranges of 10% to 20% (dashed line) and 20% to 30% (dotted line).

Figure 11 shows the optimal design when 10 angles are selected for processing at incident angles ranging from 0° to 90° at 0.5° intervals for the three porosity ranges. As porosity increases, so does the range of angles spanned by the selected angles. This increase in an-

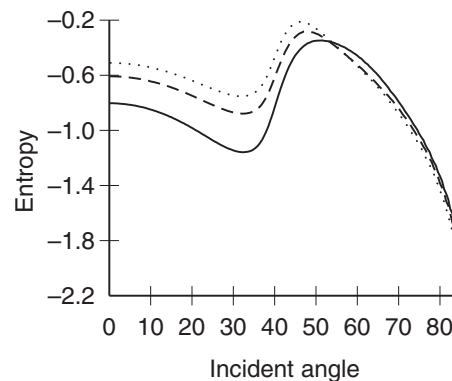


Figure 7. Entropy of  $\sigma(\mathbf{d}|\xi)$  as a function of incident angle for the general reservoir properties (Tables 1 and 2) estimated using 500,000 model-parameter samples. The brine-saturated reservoir is shown by the solid line, oil by the dashed line, and gas by the dotted line. In each case, a porosity range of 10%–40% has been used.



Figure 8. Processing design using 10 receivers placed using the Guest and Curtis (2009) method. Plot (a) represents the final design for a brine-filled reservoir, (b) an oil-filled reservoir, and (c) a gas-filled reservoir.



Figure 9. Processing design using 10 receivers placed using the Guest and Curtis (2009) method allowing only incident angles as high as 70°. Plot (a) represents the final design for a brine-filled reservoir, (b) an oil-filled reservoir, and (c) a gas-filled reservoir.

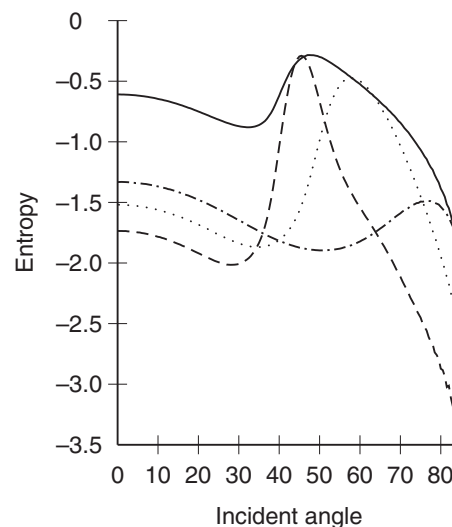


Figure 10. Entropy of  $\sigma(\mathbf{d}|\xi)$  as a function of incident angle for selecting the first trace in the different-porosity oil reservoirs to process. The solid line represents the oil reservoir with the complete prior porosity range (10% to 40%), the dashed line 10%–20% porosity, the dotted line 20%–30% porosity, and the dotted-dashed line 30%–40% porosity.

gle spread is also apparent in Figure 10, which shows that an increase in porosity broadens the information peak relating to the optimal angle. For the low-porosity model (Figure 11a), all angles are located within  $0^\circ$  to  $51^\circ$ , with each of the two angle clusters located within  $11^\circ$  envelopes. As the prior porosity range increases, so does the maximum incident angle at which an angle is selected ( $76.5^\circ$  for the 20%–30% porosity reservoir, and  $80^\circ$  for the 30%–40% porosity reservoir), as does the range over which angles are selected.

As seen in Figure 10, the 20%–30% porosity reservoir has the

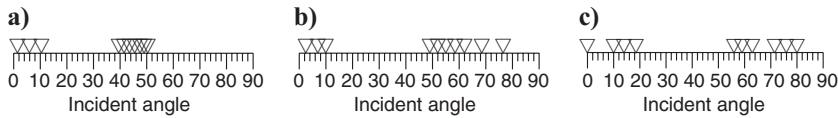


Figure 11. Processing designs for reservoir models with varying prior porosity ranges using 10 traces selected using the Guest and Curtis (2009) method. Plot (a) represents the final design for the 10%–20% porosity reservoir, (b) the 20%–30% porosity reservoir, and (c) the 30%–40% porosity reservoir. Receivers are allowed to be selected between incident angles of  $0^\circ$  and  $90^\circ$ .



Figure 12. Similar to Figure 11, but receivers are allowed to be placed between incident angles of  $0^\circ$  and  $70^\circ$ .

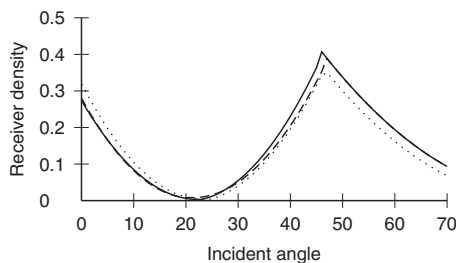


Figure 13. Receiver density plots calculated from the results in Figure 9. The regression lines shown have been fitted to  $10^\circ$  moving average results. The brine-reservoir density is shown by the solid line, the oil-reservoir density by the dashed line, and the gas-reservoir density by the dotted line.

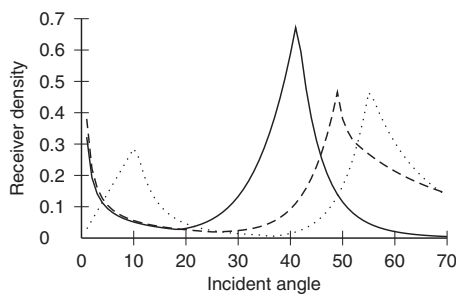


Figure 14. Receiver density plots calculated from the oil-reservoir results in Figure 12. The regression lines shown have been fitted to  $10^\circ$  moving average results. The low-porosity (10%–20%) oil-reservoir density is shown by the solid line, the medium-porosity (20%–30%) oil-reservoir density by the dashed line, and the high-porosity (30%–40%) oil-reservoir density by the dotted line.

broadest information peak; this is reflected in Figure 11b by having the largest incident angle range spanning  $49.5^\circ$  to  $76.5^\circ$ . Note that this latter range almost precludes that of the low-porosity design, again illustrating the importance of prior porosity information in AVA survey design. The relatively high importance of the near angles for the 30%–40% porosity reservoir is shown by angles being selected between  $0^\circ$  and  $20^\circ$  instead of between  $0^\circ$  and  $10^\circ$  as seen in the lower-porosity reservoirs.

Although these processing designs were found using purely computational methods, they make sense intuitively. Comparing Figure 6 and Figure 11, we see that the optimal trace-selection designs use angles so as to span (1) near-vertical incident angles and (2) the critical angle depicted in Figure 6 or (3) the highest-curvature region of Figure 6 if no critical-angle effects are observed (e.g., Figure 6c). Thus, the selected angles are sure to sample the ranges spanning the maximum variation in data values for the expected range of possible models. This strategy produces the maximum data-model sensitivity and is consistent with the expected behavior of optimal experimental design methods discussed in (Curtis 2004a, b).

Figure 12 shows the trace-selection design for the three varying porosity reservoir models if all 10 selected angles are required to be located in the incident angle range of  $0^\circ$  to  $70^\circ$ . There is no change in the 10%–20% porosity reservoir because all selected angles in Figure 11a were located at angles less than  $70^\circ$ . The two other trace-selection designs show no change in the near-offset selected angle positions. At large offsets, the closest selected angle remains the same, with the remaining angles more closely spaced and a single selected angle at the maximum offset of  $70^\circ$ . Although Figure 10 shows that small angles for a high-porosity reservoir correspond to the largest entropy values for a single selected angle, the final 10-angle design (Figure 12c) locates the majority of the angles at large offsets, a result unobtainable by considering only the single-angle entropy plot shown in Figure 10.

## DISCUSSION

Although the 10-angle results shown do not constitute an industrial-sized processing design, the use of 10 angles is sufficient to determine the receiver-density profile along a full seismic survey to approximately maximize the information recorded for any set number of selected receivers. Figure 13 shows regression receiver-density curves fitted to the  $10^\circ$  moving average angle results calculated from Figure 9. As shown in Figure 9, the angle density plots are very similar for all three saturating fluids. The density value peaks at about  $50^\circ$ , corresponding to the information peak shown in the single-angle information curve (Figure 7). The density plot also shows a decreasing angle density pattern between  $0^\circ$  and  $20^\circ$ . The density is minimum at angles of about  $10^\circ$  to  $35^\circ$ , which corresponds to the range void of selected angles shown in Figure 9.

Figure 14 shows the density result calculated from the angle positions in Figure 12 for oil-saturated reservoirs with different porosities. It is clear that designing an optimal angle-density processing profile for a reservoir is far more dependent on the reservoir porosity information than on information about the saturating fluid properties. For high-porosity values (dotted line in Figure 14), a larger pro-

portion of the selected angles to be processed should be placed at low incident angles, around  $10^\circ$ , and as porosity decreases, the highest density range also shifts to lower angles. For all cases, however, there is a density minimum around  $30^\circ$ .

Although the trace-selection designs shown in Figure 11 are intuitive retrospectively given Figure 6 — and indeed, Figure 6 might be used to estimate the qualitative features of optimal trace-selection designs — Figure 6 could not be used to create the exact processing designs themselves because the precise optimal angle-density curves (Figure 13 and Figure 14) cannot be estimated from Figure 6 directly. Hence, the sophisticated SED methods that we present are necessary.

These density profiles can be interpreted in several ways, depending on how the recorded data are to be used. If all the traces are to be analyzed using AVA/AVO methods, then the density results indicate which traces require the most attention preanalysis so as, for example, to remove sources of noise and multiples. Receivers with large density values require the most effort because those traces will provide the most information on subsurface parameters. Traces corresponding to low densities provide little extra AVA information, and time spent removing noise from the data might be proportionally reallocated to more important tasks. If only a subset of receivers is to be processed, then the density indicates the densities of traces that should be selected to best constrain the subsurface parameters of interest.

Rather than selecting single traces, a more robust approach would be to select and process groups of traces in some small angle or offset range around each of the optimal locations found, perhaps combining the results of each group into a single AVA datum, using the stacking power of each group to reduce random noise in the datum. Both of those methods result in significant computational or time savings compared to standard methods. In the first method, the amount of time preanalysis is reduced to a minimum by concentrating only on data that contain useful information. In the second method, the processing time is reduced to a minimum by considering only an optimal subset of (groups of) the data.

Although optimal receiver-selection profiles have been presented, the amount of extra information provided compared to that from a standard design has not been quantified. Figure 15 shows the expected increase in information gain on the subsurface parameters by using the optimal trace selection over the standard constant spatial-receiver separation for a medium-porosity oil reservoir located at 500-m depth with a homogeneous overburden. Both the optimal trace-selection design and the constant spatial-separation trace-selection designs place the majority of the receivers at large angles. When only a few groups of receivers are used, the expected information gain is very high. Figure 15 shows that as more receiver groups are selected, the expected information gain falls but always remains greater than 14%. By using the concept that the results relate to receiver groups rather than to individual traces, a processing design using only three groups (which could consist of hundreds of individual traces) would produce expected gains of 35%.

Figure 15 agrees with the idea of “diminishing returns,” which postulates that as the number of receivers increases, the relative advantage of using optimal designs over standard designs decreases (Coles and Morgan, 2009). The highest-value niche for these design methods clearly occurs when we focus attention on relatively small portions of the data set, e.g., for rapid or low-cost AVA analysis. Indeed, these design methods might significantly facilitate such applications.

Because the algorithm calculates the optimal incident angles at the caprock/reservoir boundary, it is easy to transform the results into specific cases with more complex geometry. Figure 16 shows the actual source-receiver offset profiles rather than incident angle, which correspond to the optimal offset selection designs for different interface depths and subsurface properties. (The solid line represents a 20%–30% porosity interface at 500-m depth and the dotted line a 30%–40% porosity interface at 1000-m depth. In each case, a homogeneous overburden model has been used.)

Although the design may change if layers dip instead of being horizontal, the algorithm that we use to calculate optimal designs still would be robust. This is because we calculate the optimal distribution of incident angles at the reflector to be analyzed. Whatever distribution of angles is found can be traced back to the surface through the overburden model, as shown in Figure 17, to find optimal sensor locations on the surface.

In certain scenarios, only a limited design space may be available from which to select traces because of logistics of the data collection or the methods used to process the data. In these cases, the same methods described above can be used by calculating only the information value over the relevant design-space regions. It is also common practice to bin data into certain angle ranges, averaging the AVA response in each bin, resulting in lower uncertainties on the mean AVA data within each bin. In such cases, lower expected data uncertainties can be used in the methods described above, and the optimal angles found in the previous examples can be regarded as optimal bin-center locations.

In many realistic situations, data uncertainty might increase with offset. In our methodology, we consider only constant error with respect to offset. In future work, it might be beneficial to add variable uncertainties so that information provided by far offsets is weighted

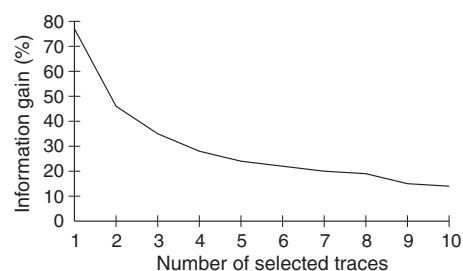


Figure 15. Information gain expected by processing the optimal trace selection compared to selecting evenly spaced receiver traces for a medium porosity oil reservoir at 500-m depth as a function of the total number of receivers used.

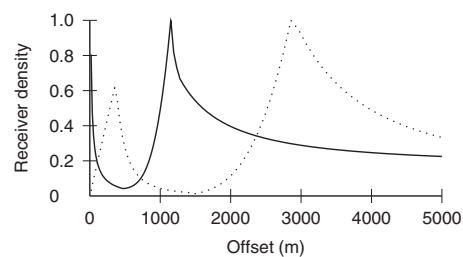


Figure 16. Normalized receiver density plots as a function of surface offset for a high-porosity (30%–40%) oil reservoir at 1000-m depth (dotted line) and a medium-porosity (20%–30%) oil reservoir at 500-m depth (solid line).

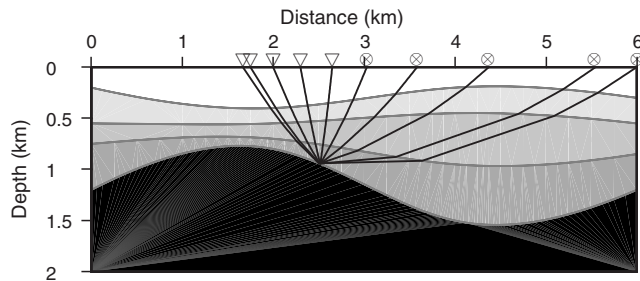


Figure 17. Raypaths calculated from five optimal angles located at a dipping interface. Tracing the optimal angles to the surface allows the properties of the complex overburden to be taken into consideration when transforming the optimal angles to optimal source-receiver offsets. Source locations are shown by  $\otimes$  and receivers by  $\nabla$ . Gray shading represents velocity, with darker shades corresponding to faster velocities.

with respect to near offsets which provide measurements with relatively low error. Alternatively, the designs above are approximately correct if bin-widths increase with offset so that the uncertainties on amplitudes after stacking results within the bin are roughly equal for each bin.

Although our presentation of the new techniques has been targeted at how to optimize processing of AVO data by selecting which receivers from a regularly spaced data set should be processed to extract the maximum amount of information, the same principles can be used to design the actual data-collection survey with receivers located only at offsets which are expected to record maximum information about the subsurface. In this way, unnecessary data are not recorded, and all the data can be processed with the knowledge that the data set being processed is optimal.

## CONCLUSIONS

Using an iteratively constructive design method in conjunction with a semiempirical petrophysical model, several optimal AVA trace-selection processing designs have been presented for reservoirs with differing saturating fluids and porosity ranges. It has been shown for a range of subsurface models that reducing the prior uncertainty on the estimate of the reservoir porosity has a far greater influence on the resulting trace-selection designs than has prior knowledge about the saturating-fluid properties.

Using the optimal trace-selection designs thus found to create receiver-density profiles, large-scale seismic-survey data-processing profiles can be designed specifically for subsurface horizons of interest. By running the trace-selection algorithm for different targets of interest, optimal processing receiver-density profiles can be created which can be applied to the same original data set to ensure that for each interface, the maximum information is inferred for the lowest processing effort and cost.

## ACKNOWLEDGMENTS

Thanks are extended to Schlumberger for permission to publish this work. We acknowledge the support from the Scottish Funding Council for the ECOSSE Joint Research Institute, part of the Edinburgh Research Partnership in Engineering and Mathematics (ER-Pem). Herbert Swan and two anonymous reviewers are thanked for their comments, which helped to improve the manuscript.

## REFERENCES

- Ajo-Franklin, J., 2009, Optimal experiment design for time-lapse traveltime tomography: *Geophysics*, **74**, no. 4, Q27–Q40.
- Atkinson, A., and A. Donev, 1992, *Optimum experimental designs*: Oxford Science Publications.
- Barth, N., and C. Wunsch, 1990, Oceanographic experiment design by simulated annealing: *Journal of Physical Oceanography*, **20**, 1249–1263.
- Box, G., and H. Lucas, 1959, Design of experiments in non-linear situations: *Biometrika*, **46**, 77–90.
- Carcione, J., H. Helle, N. Pham, and T. Toverud, 2003, Pore pressure estimation in reservoir rocks from seismic reflection data: *Geophysics*, **68**, 1569–1579.
- Chen, J., and T. A. Dickens, 2009, Effects of uncertainty in rock-physics models on reservoir parameter estimation using seismic amplitude variation with angle and controlled-source electromagnetics data: *Geophysical Prospecting*, **57**, 61–74.
- Clark, V., 1992, The effect of oil under in-situ conditions on the seismic properties of rocks: *Geophysics*, **57**, 894–901.
- Coles, D., and F. Morgan, 2009, A method of fast, sequential experimental design for linearized geophysical inverse problems: *Geophysical Journal International*, **178**, 145–158.
- Curtis, A., 1999a, Optimal design of focused experiments and surveys: *Geophysical Journal International*, **139**, 205–215.
- , 1999b, Optimal experiment design: Cross-borehole tomographic examples: *Geophysical Journal International*, **136**, 637–650.
- , 2004a, Theory of model-based geophysical survey and experimental design: Part 1 — Linear problems: *The Leading Edge*, **23**, 997–1004.
- , 2004b, Theory of model-based geophysical survey and experimental design: Part 2 — Nonlinear problems: *The Leading Edge*, **23**, 1112–1117.
- Curtis, A., and H. Maurer, 2000, Optimizing the design of geophysical experiments: Is it worthwhile?: *The Leading Edge*, **19**, 1058–1062.
- Curtis, A., A. Michelini, D. Leslie, and A. Lomax, 2004, A deterministic algorithm for experimental design applied to tomographic and microseismic monitoring surveys: *Geophysical Journal International*, **157**, 595–606.
- Curtis, A., and R. Wood, 2004, Optimal elicitation of probabilistic information from experts, in A. Curtis and R. Wood, eds., *Geological prior information: Informing science and engineering*: Geological Society [London] Special Publication 239, 127–145.
- Downton, J., and C. Ursenbach, 2006, Linearized amplitude variation with offset (AVO) inversion with supercritical angles: *Geophysics*, **71**, no. 5, E49–E55.
- Furman, A. T., P. A. Ferré, and G. Heath, 2007, Spatial focusing of electrical resistivity surveys considering geologic and hydrologic layering: *Geophysics*, **72**, no. 2, F65–F73.
- Furman, A., T. P. A. Ferré, and A. W. Warrick, 2004, Optimization of ERT surveys for monitoring transient hydrological events using perturbation sensitivity and genetic algorithms: *Vadose Zone Journal*, **3**, 1230–1239.
- Goldberg, I., and B. Gurevich, 1998, A semi-empirical velocity-porosity-clay model for petrophysical interpretation of P- and S-velocities: *Geophysical Prospecting*, **46**, 271–285.
- Guest, T., and A. Curtis, 2009, Iteratively constructive sequential design of experiments and surveys with nonlinear parameter-data relationships: *Journal of Geophysical Research*, **114**, B04307.
- Kijko, A., 1977a, An algorithm for the optimal distribution of a regional seismic network — 1: Pure and Applied Geophysics, **115**, 999–1009.
- , 1977b, An algorithm for the optimum distribution of a regional seismic network — 2: An analysis of the accuracy of location of local earthquakes depending on the number of seismic stations: *Pure and Applied Geophysics*, **115**, 1011–1021.
- Lindley, D., 1956, On a measure of the information provided by an experiment: *Annals of Mathematical Statistics*, **27**, 986–1005.
- Liu, Y., and D. Schmitt, 2003, Amplitude and AVO responses of a single thin bed: *Geophysics*, **68**, 1161–1168.
- Macdonald, C., P. Davis, and D. Jackson, 1987, Inversion of reflection travel-times and amplitudes: *Geophysics*, **52**, 606–617.
- Marion, D., A. Nur, H. Yin, and D. Han, 1992, Compressional velocity and porosity in sand-clay mixture: *Geophysics*, **57**, 554–563.
- Maurer, H., and D. Boerner, 1998, Optimized design of geophysical experiments: *The Leading Edge*, **17**, 1119–1125.
- Maurer, H., D. Boerner, and A. Curtis, 2000, Design strategies for electromagnetic geophysical surveys: *Inverse Problems*, **16**, 1097–1117.
- Mavko, G., T. Mukerji, and J. Dvorkin, 1998, *The rock physics handbook*: Cambridge University Press.
- Oldenborger, G., and P. Routh, 2009, The point-spread function measure of resolution for the 3-D electrical resistivity experiment: *Geophysical Journal International*, **176**, 405–414.
- Oldenborger, G., P. Routh, and M. Knoll, 2007, Model reliability for 3D electrical resistivity tomography: Application of the volume of investigation index to a time-lapse monitoring experiment: *Geophysics*, **72**, no. 4, F167–F175.

- Ostrander, W., 1984, Plane-wave reflection coefficients for gas sands at non-normal angles of incidence: *Geophysics*, **49**, 1637–1648.
- Rabinowitz, N., and D. Steinberg, 2000, A statistical outlook on the problem of seismic network configuration, in C. Thurber and N. Rabinowitz, eds., *Advances in seismic event location*, Kluwer Academic Publishers Modern Approaches in Geophysics, 18, Ch. 30.
- Shannon, C., 1948, A mathematical theory of communication: *Bell System Technical Journal*, **27**, 623–656.
- Shewry, M. C., and H. P. Wynn, 1987, Maximum entropy sampling: *Journal of Applied Statistics*, **14**, 165–170.
- Skopintseva, L., and T. V. Nefedkina, 2006, AVO-inversion for postcritical reflections: 68th Conference and Exhibition, EAGE, Extended Abstracts, P058.
- Steinberg, D., N. Rabinowitz, Y. Shimshoni, and D. Mizrahi, 1995, Configuring a seismographic network for optimal monitoring of fault lines and multiple sources: *Bulletin of the Seismological Society of America*, **85**, 1847–1857.
- Stummer, P., H. Maurer, and A. Green, 2004, Experimental design: Electrical resistivity data sets that provide optimum subsurface information: *Geophysics*, **69**, 120–139.
- Tarantola, A., 2005, Inverse problem theory and methods for model parameter estimation: Society of Industrial and Applied Mathematics.
- van den Berg, J., A. Curtis, and J. Trampert, 2003, Optimal nonlinear Bayesian experimental design: An application to amplitude versus offset experiments: *Geophysical Journal International*, **155**, 411–421, Errata: 2005, *Geophysical Journal International*, **161**, 265.
- Wilkinson, P., P. Meldrum, J. Chambers, O. Kuras, and R. Ogilvy, 2006, Improved strategies for the automatic selection of optimized sets of electrical resistivity tomography measurement configurations: *Geophysical Journal International*, **167**, 1119–1126.
- Williams, R., G. Roberts, and K. Hawkins, 2001, Long offset towed streamer recording — A cheaper alternative to multi-component OBC for exploration?: *Exploration Geophysics*, **32**, 316–319.
- Winterfors, E., and A. Curtis, 2008, Numerical detection and reduction of non-uniqueness in nonlinear inverse problems: *Inverse Problems*, **24**, 025016.
- Zoeppritz, K., 1919, On the reflection and penetration of seismic waves through unstable layers: *Göttinger Nachrichten*, **1**, 66–84.